Radiation Physics and Chemistry 166 (2020) 108497

Contents lists available at ScienceDirect

Radiation Physics and Chemistry

journal homepage: www.elsevier.com/locate/radphyschem

Preparation and characterization of zinc, lanthanum white sand glass for use in nuclear applications

A.M. El-Khayatt[a,b], H.A. Saudy[c,*]

[a] Department of Physics, College of Science, Imam Mohammad Ibn Saud Islamic University, (IMSIU), Riyadh, Saudi Arabia
[b] Reactor Physics Department, Nuclear Research Centre, Atomic Energy Authority, 13759, Cairo, Egypt
[c] Department of Physics, Faculty of Science, Al-Azhar University, Women Branch, Nasr City, Cairo, Egypt

ARTICLE INFO

Keywords:
Silica
Microhardness
Mass attenuation coefficients
Radiation shielding

ABSTRACT

Glass derived from natural sand such as the white Sinai sand (WSS) is considered to be natural glass. It is known for its remarkable properties that exhibits excellent mechanical properties. Six natural glass networks had been prepared using the melt quenching method. The structural properties of the prepared samples were investigated by the X-ray diffraction (XRD) technique. Optical properties the glasses were evaluated by the UV–visible absorption measurements. Glass systems were evaluated for density, molar volume (V_M), oxygen molar volume (V_O), oxygen packing density (POD), and radiation properties according to the substitution of ZnO by La_2O_3. The mass attenuation coefficients (μ_m), effective atomic numbers (Z_{eff}) and gamma-ray kerma coefficients (k) of the glasses at different photon energies were determined experimentally and calculated theoretically. The obtained results have shown that the current glasses have superior shielding properties compared to basalt magnetite concrete (BMC) and steel scrap concrete (SSC) as standard radiation shielding materials. The substitution of ZnO by La_2O_3 improves all gamma-ray attenuation parameters by about 20–29%. Moreover, the attenuation of neutrons was discussed in terms of the macroscopic removal cross-section (Σ_R) and the glasses were found to have better neutron radiation shielding properties than SSC and BMC. These findings have demonstrated that the present glass systems can be suitably used as a shielding material at sites of the nuclear and X-ray facilities.

1. Introduction

The most standard nuclear radiation shielding material is concrete as a result of its low price and flexibility for any construction vogue. However, there are several restrictions connected to victimization concrete as a radiation shielding material (Un and Demir, 2013; Alallak and Sarhan, 2012). Lead is another most used radiation shielding material, but it is much more expensive than either concrete or glass, besides, it's opaque. The most necessary advantage of using glass as a shielding material in addition to its transparency is that many different compositions can be prepared to achieve this goal (Kaundal, 2016). The glasses supported two or more network formers have found great attention in the scientific material with technological promises.

Borate and silica glasses are interesting hosts due to their remarkable characteristics (Oliveira, 2008). Glasses doped with lanthanide component area units are those materials which have high potential and applied in many fields, including laser applications, amplifier, and optical devices (Singh et al., 2014). Lanthanum plays a significant role in the manufacture of radiation shielding glass and acts as a network modifier, the kernel agent will improve the stability of glass by forming the ionic bonds with the non-bridging oxygen (Singh et al., 2017). Furthermore, the glasses containing lanthanide ions aren't luminescent however conjointly act as scintillators conjointly below ionizing radiation. The presence of rare earths within the glasses will increase the radiation hardness (Singh et al., 2014).

Attenuation of γ-rays is being represented by many parameters such as mass attenuation coefficient (μ_m), half-value layer (HVL), atomic cross-section (σ_a), electronic cross-section(σ_e), effective atomic number (Z_{eff}), and effective electron density (N_{eff}). As the mass attenuation coefficient is the fundamental attenuation parameter, it can be used to estimate the other parameters as described in literatures (Junior et al., 2017; Limkitjaroenporn et al., 2013; El-Khayatt and Akkurt, 2013).

Gamma-ray heating is the local energy deposition from gamma-ray interactions. Often this can be done by estimating the kerma (K). The fluence-to-kerma conversion coefficient or “kerma coefficient” (k) (in Gy.cm^2/photon) converts the radiation passing through a unit volume of a material of interest (fluence) to the energy release (kerma, K) in the material. So kerma coefficient can be considered as the key response

* Corresponding author.
E-mail address: heba_saudi@azhar.edu.eg (H.A. Saudy).

https://doi.org/10.1016/j.radphyschem.2019.108497
Received 24 June 2019; Received in revised form 6 September 2019; Accepted 17 September 2019
Available online 21 September 2019
0969-806X/

function for nuclear heating and it is particularly important in many nuclear applications such as fission and fusion power reactors (Zhang and Abdou, 1997). k is also of benefit for biomedical applications in terms of absorbed dose from uncharged particles fluence (Liu and Chen, 2008; El-Khayatt and Vega-Carrillo, 2015). El-Khayatt (2017) reported a method for estimating experimental values for kerma coefficients from experimental mass attenuation coefficients.

Many authors have reported radiation attenuation parameters of heavy metal oxides borosilicate glasses (Alharbi et al., 2019), lithium borate glasses doped with minerals (Esra, 2019), lead-bismuth glasses (Abouhaswa et al., 20199), tellurite glasses (Sayyed et al, 2019), borosilicate glasses (Saddeek et al., 2018), silicate glasses (Kirdsiri et al., 2011), and gadolinium based oxide glasses (Shamshad et al, 2017). However, each glass system has its own physical characteristics and shielding properties that are defined by a unique combination of these factors. This encouraged us to prepare the current glasses as a potential shielding against gamma and fast neutron. Therefore, we have measured and calculated the mass attenuation coefficients, half-value layer, effective atomic numbers, effective electron densities, and kerma coefficients of white sand glasses containing zinc and lanthanum as given in Table 1. Additionally, the attenuation of fast neutrons in the energy range (2–12 MeV) was evaluated in terms of the macroscopic removal cross-section neutron (Σ_R). In the present work, the physical and radiation properties for the glass network fabricated from Sinai white sand (WSS) were investigated according to the substitution of ZnO by La_2O_3. The study can be useful for radiation shielding design purposes.

2. Material and methods

2.1. Sample preparation

Firstly, a representative sample of the WSS was analyzed for composition by the X-ray diffraction (XRD) technique. The results showed that it was primarily composed of SiO_2 (90.4%), CaO (3.8%), ZrO_2 (2.3%), Fe_2O_3 (2.1%). i.e. the powder obtained from WSS contains 90.4% SiO_2.

A series of glasses with the chemical composition [xLa_2O_3(40-x) ZnO10Na_2O10$B_2O_3$40 WSS] where x = 0, 6, 12, 18, 24 and 30 wt%) have been fabricated using the conventional rapid melt quenching method. An appropriate amount of the sand has been milled to a very fine level (powder) were used for a 30 g batch/melt. The starting chemical materials were weighed with the help of a 4-digit sensitive microbalance to obtain the required configuration and grind them completely in a porcelain agate mortar. Batches of 30 g were melted in a porcelain crucible in a temperature range of 1150–1200 °C with heating rate of 5 °C/min. The melt of each composition was poured into a heavy steel mold that is quickly pressed by the aluminum plate and immediately moves to a preheated oven to heat at 450 °C and left it cool to room temperature inside the oven. All in all, they are six glasses in this study and they noted throughout the paper as follows; S, S1, S2, S3, S4 and S5, which corresponded to x = 0, 6, 12, 18, 24 and 30 wt%. Finally, glass samples are obtained in circular form of 2.5 cm. Photos for representative samples of each type of prepared glass are shown in Fig. 1.

Table 1
Chemical composition (wt%) of the prepared glasses.

Constituent	X = 0	X = 6	X = 12	X = 18	X = 24	X = 30
	S	S1	S2	S3	S4	S5
SiO_2	36.16	36.16	36.16	36.16	36.16	36.16
UO_2	0.56	0.56	0.56	0.56	0.56	0.56
ZrO_2	0.92	0.92	0.92	0.92	0.92	0.92
Fe_2O_3	0.84	0.84	0.84	0.84	0.84	0.84
CaO	1.52	1.52	1.52	1.52	1.52	1.52
La_2O_3	0	6	12	18	24	30
ZnO	40	34	28	22	16	10
Na_2O	10	10	10	10	10	10
B_2O_3	10	10	10	10	10	10

The amorphous nature of all the prepared samples has been confirmed by the absence of Bragg's peak in X-ray diffraction (XRD) pattern. As well as their chemical compositions are listed in Table 1.

2.2. 2. Density measurements

The density of glass samples was measured at room temperature by Archimedes principle using Toluene as immersion liquid. Toluene was chosen because its superior chemical stability against hygroscopic attack of the glass and its toxicity is relatively low. Based on Archimedes principle, the density (ρ) of the glasses can be determined by the following relation:

$$\rho = \frac{W_a}{W_a - W_b}\rho_{Toluene} \quad (1)$$

where W_a is the weight in air; W_b is the weight in Toluene; $\rho_{Toluene}$ is the density of Toluene at room temperature ($\rho_{Toluene}$ = 0.8669 g /cm^3). The corresponding molar volume (V_M), oxygen molar volume (Vo) and oxygen packing density (OPD), were calculated using the relations;

$$V_M = \frac{M}{\rho}, \quad (2)$$

$$V_O = V_M \frac{1}{n}, \quad (3)$$

$$OPD = 1000\frac{\rho}{M}n. \quad (4)$$

where M is the total molecular mass of the multi-component glass system, and n is the number of oxygen atoms per formula unit.

2.3. Surface properties (Vickers hardness)

A Vicker's diamond indenter was employed in a customary microhardness tester (Leco AMH one hundred, USA) for specimen indentation. A load of five hundred grams applied for 20 s was accustomed build indentations in specimens of glasses. Every sample was subjected to 5 indentations at arbitrarily selected areas; therefore, errors in the measured values corresponding to the quality deviation are regarding 4%. The diagonal length impressions were measured and also the hard range Hv was calculated consistent with a custom formula: H = 1.854 P/d^2 kg/mm^2, wherever P is that the indentation load, and d is that the diagonal length impression (Saudy et al., 2013).

2.4. Measurement of mass attenuation coefficients μ_m

A narrow beam γ-ray transmission geometry was employed for the gamma-ray attenuation measurements. The block diagram of the experimental set-up for the measurement of the mass attenuation coefficient (μ_m) is presented in Fig. 2. A scintillation 2″ × 2″ NaI (TI) detector with energy resolution of 12.5% at 662 keV coupled with multi-channel analyzer (MCA). Samples were placed on the specimen holder at a distance of 10 cm from the source. The space between source and detector was 19 cm. The γ-emitter radioactive sources, ^{133}Ba, ^{60}Co and ^{137}Cs, have been used for irradiation process as well as for energy and efficiency calibration of the detector.

Incident and transmitted intensities of photons were measured by MCA for fastening planned time for every sample by choosing a slim region symmetrical with reference to the center of mass of the photopeak. The measured photo-peaks were normalized to the count rate measured without glass for all energies. Hence, linear attenuation coefficients μ can be estimated by Beer-Lambert's law

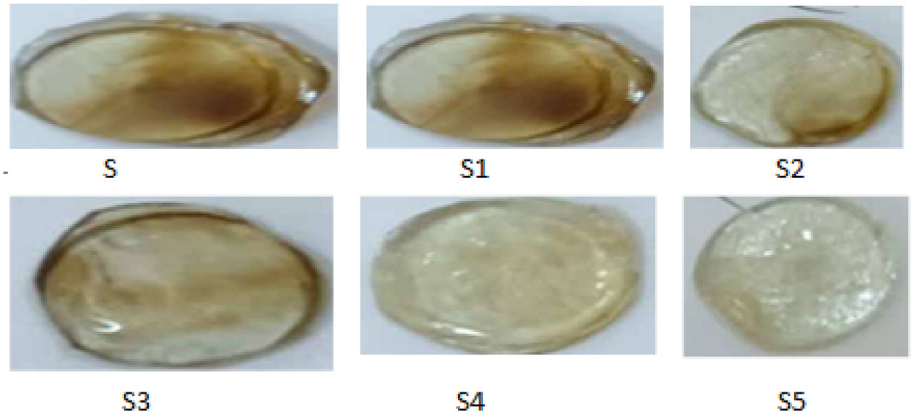

Fig. 1. Photos for representative samples of each type of prepared glass.

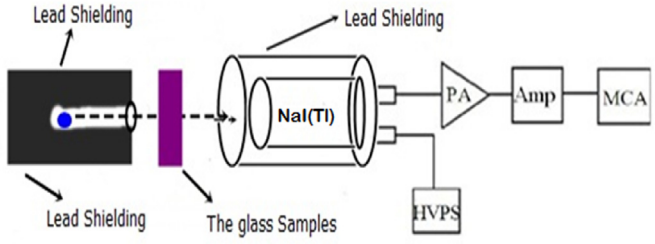

Fig. 2. The block diagram of narrow beam transmission geometry for the measurement of mass attenuation coefficient (μ_m).

$$\mu = \frac{1}{x}\ln(I_0/I), \tag{5}$$

where x is the material thickness (cm); I_0 and I are the area under photo-peaks of incident and transmitted photons, respectively.

Since the linear attenuation coefficient varies with the density of absorbing medium, its use is limited. Therefore, the mass attenuation coefficient, $\mu_m = \mu/\rho$, is used much more widely in shielding calculations which given by

$$\mu_m = \frac{1}{t}\ln(I_0/I), \tag{6}$$

where t is the sample mass thickness (areal density in g/cm^3).

For a given photon energy, we plot $\ln(I_o/I)$ as a function of thickness for all glasses, then accurate values for μ_m are obtained from the plots by linear regression. In all cases the statistical errors in counting rates were kept to less than 1%.

The maximum total standard error in mass attenuation coefficients $\Delta(\mu_m)$ has been calculated from errors in incident (I_0) and transmitted (I) intensities and areal density (t) using the propagation of error formula (Singh et al., 2008)

$$\Delta(\mu_m) = \frac{1}{t}\sqrt{\left(\frac{\Delta I_o}{I_o}\right)^2 + \left(\frac{\Delta I}{I}\right)^2 + \left(\ln\frac{I_o}{I}\right)^2\left[\left(\frac{\Delta\rho}{\rho}\right)^2 + \left(\frac{\Delta t}{t}\right)^2\right]} \tag{7}$$

where ΔI_o, ΔI, $\Delta\rho$ and Δt are the errors in the intensities I_o, I, density ρ and thickness t of the sample, respectively. Estimated error in the experimental measurement was less than 3%.

On the other hand, the theoretical mass attenuation coefficients of the glass samples can be calculated using WinXCom program in the energy range from 1 keV to 100 GeV (Gerward et al, 2004). This program is based on the additive "Mixture Rule" (Hubbell and Seltzer, 1995). Therefore:

$$(\mu_m)_{glass} = \sum_i w_i(\mu_m)_i, \tag{8}$$

where w_i and $(\mu_m)_i$ are weight fraction and mass attenuation coefficient of the individual constituent element i.

Based on mass attenuation coefficients, theoretically and experimentally additional radiation shielding parameters, such as half value layer (HVL), effective atomic number, Z_{eff} (electron/atom), kerma coefficients k (Gy.cm^2/photon) for the range of 1 keV–1000 MeV have been determined.

In this study, the authors followed the same procedure for the measurement and calculation of μ_m, HVL, Z_{eff} and k shielding parameters used in the earlier studies conducted by (Junior et al., 2017; Limkitjaroenporn et al., 2013; El-Khayatt and Akkurt, 2013; El-Khayatt, 2017).

2.5. Macroscopic effective removal cross-section for fast neutrons (Σ_R)

The shielding material should have a proper ratio of heavy to light elements; low Z-material ($A \leq 16$) used to moderate the neutron and high Z-material for the gamma-ray attenuation. In shielding calculation, the macroscopic effective removal cross-section for fast neutrons, simply removal cross-section, Σ_R, can be considered as a given probability of the large angle scattering (both elastic and inelastic), which would tend to remove the neutron from the group of penetrating, uncollided neutrons (Blizard and Abbott, l962). The Σ_R for glass can be calculated in the energy range (2–12 MeV) from the value Σ_R or Σ_R/ρ for various elements by the following expressions (Kaplan, 1989):

$$(\Sigma_R)_{glass} = \sum_i \rho_i(\Sigma_R/\rho)_i, \tag{9}$$

$$(\Sigma_R/\rho)_{glass} = \sum_i w_i(\Sigma_R/\rho)_i. \tag{10}$$

where ρ_i and $(\Sigma_R/\rho)_i$ are the partial density and the mass removal cross-section of the ith constituent, respectively.

3. Results and discussion

3.1. The X-ray diffraction patterns

A typical XRD spectra for three glass samples are shown in Fig. 3. No Bragg's peaks are observed in all spectra, which confirm the non-crystalline (glassy) nature of the prepared samples.

3.2. Glass density and the related physical parameters

The physical and structural properties of the glasses were investigated by measuring the densities of the glass samples. The dependence of glass density (ρ) on the lanthanum oxide content is shown in Fig. 4. The density of the current glasses is found to be within the range from 3.9 to 4.18 g cm^{-3} as listed in Table 2. It can be observed that the density increased linearly with an increase in La_2O_3 content.

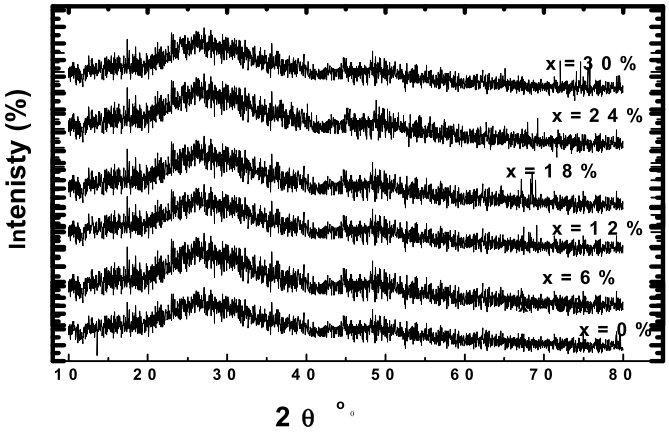

Fig. 3. XRD patterns at room temperature for prepared glass samples.

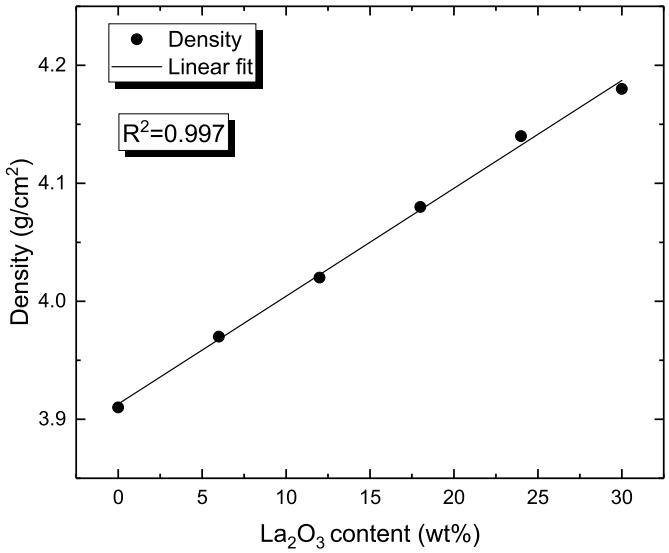

Fig. 4. Variation of glass density with lanthanum oxide content.

Table 2
The measured density, molar volume, oxygen molar volume and oxygen packing density of various glasses.

Glass	Composition (wt %)					ρ	V_M	OPD	V_O
	La_2O_3	ZnO	Na_2O	B_2O_3	WSS	g/cm^3	g/mol	mol/cm^3	cm^3/mol
S	0	40	10	10	40	3.914	17.74	91.95	10.88
S1	6	34	10	10	40	3.968	18.20	92.48	10.81
S2	12	28	10	10	40	4.022	18.70	93	10.75
S3	18	22	10	10	40	4.076	19.25	93.5	10.7
S4	24	16	10	10	40	4.130	19.86	93.97	10.64
S5	30	10	10	10	40	4.184	20.54	94.43	10.59

This outcome was expected, because La_2O_3 possesses a higher specific density (6.51 g/cm^3) in comparison to the ZnO (5.61 g/cm^3). Consequently, the unit weight of the glass system increases as the percentage of La_2O_3 content increases.

Table 2 lists the structural parameters which estimated from the glass density, such as V_m, V_O and OPD. The values of V_m and OPD increase with increasing La_2O_3 content, whereas the values of Vo decrease with increasing La_2O_3 content. These findings were expected, as a result of the ionic radius of La^{3+} (0.1061 nm) is larger than the ionic radius of Zn^{2+} (0.074 nm). Moreover, the increase of the oxygen packing density (OPD) indicated more tightly packing of the glass network (Smiljanić et al, 2015). Therefore, it can be concluded that

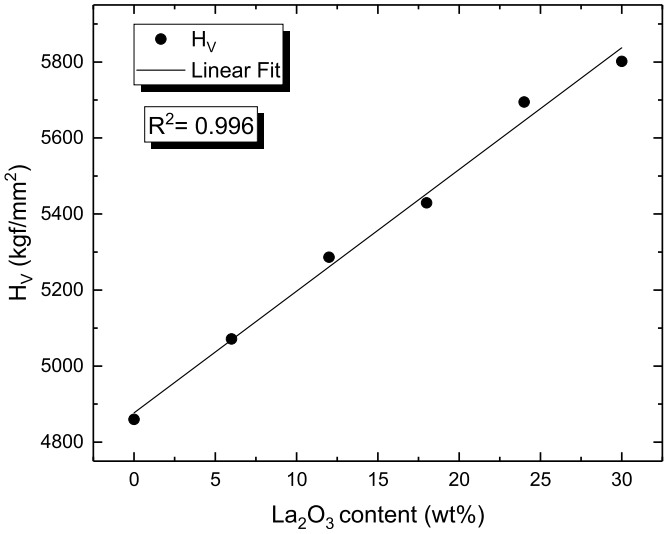

Fig. 5. Hardness values, H_V, versus lanthanum oxide content for the studied glasses (at 500 g during 20 s in ambient conditions).

replacement ZnO by La_2O_3 helps to improve tightly packing of the glass system.

3.3. Surface properties (Vickers hardness)

Vickers hardness was measured using polished samples of the glasses under investigation in the form of a circle ≈ 0.5 cm thick on a microhardness tester equipped with a tetrahedral diamond pyramid with an apex angle of 136°, and calculated hardness number H_v of current glasses.

The indentation hardness data where the hardness number H_v is plotted versus the La_2O_3 content is shown in Fig. 5. As the La_2O_3 content increase, the hardness number Hv increased with the applied load = 500 g at the loading time = 20s. The microhardness of the glass depends on the strength of chemical bonds in the solid and that the microhardness is related to the parameters of the hole theory, the formation of indentations during the microhardness test of glasses can be treated as a result of the disappearance of "holes"in the micro volume under the indenter, which leads to a densification of the material. The increase in hardness in the current glass is due to the relatively high sand content of 40%. The WSS contains the calcium and iron oxides (as mentioned before) which make the glass denser and more rigid. They increase the coherence of its chemical bonds and reduces the gaps between them (Saudy et al., 2013).

3.4. Optical properties

The transmittance of these glasses has been evaluated by the UV–visible absorption measurements. Transmission spectra of the prepared glasses in the range 190–1100 nm were measured by Genway 6405 -UV-VIS spectrophotometer.

The UV and visible transmission spectra for all prepared samples follow one common pattern as shown in Fig. 6. Also, the extended edge is over the wide wavelength, which corresponds to the non-crystalline nature of the glasses. The cut-off wavelength (λ_c) exhibit red shift with increased content of La_2O_3. Such behavior can be calculated by increasing the number of non-bridging oxygen. The same behavior was observed by increasing ZnO content in bismuth borate glass (Kim et al., 2009). A shoulder at 661 nm was observed and expanded with increased La_2O_3 content. It is clear from the figure that, the transmission ratio increases gradually with increasing the content of La_2O_3 where all samples containing La_2O_3 show high percentage of transmittance in the visible area of spectra (650 nm–1000 nm) exceeds 80% when the La_2O_3

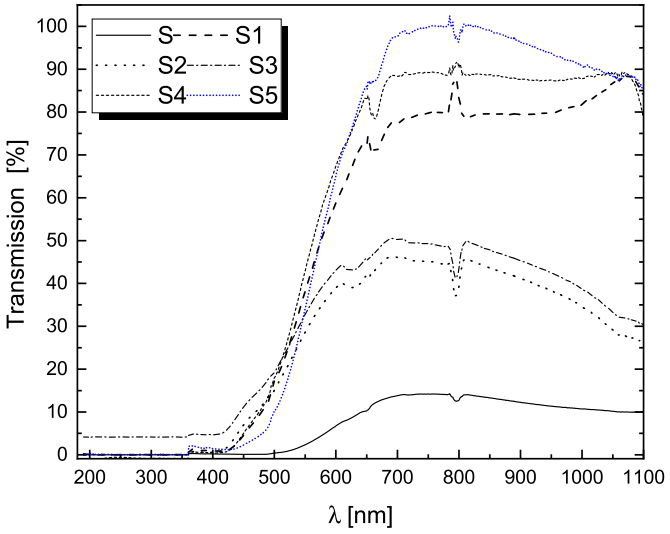

Fig. 6. Optical transmittance, as a function of wavelength (nm), of the prepared glasses.

content is x = 30%. Moreover, the sample containing 18% La_2O_3 shows a strong absorption in the UV area reaches 550 nm Thus, we can say that the current glass is transparent and allows visibility behind it, where the glass containing La_2O_3 may serve as a kind of absorbent of laser camouflage material.

3.5. Gamma-ray shielding parameters

Weight fractions were calculated based on the chemical composition of all glasses as shown in Table 1. These fractions were used as input data for WinXCom to calculate the μ_m for all samples. The obtained data of the experimental and theoretical μ_m of the glasses have been converted into half value layer (HVL), effective atomic number (Z_{eff}) and gamma-ray kerma coefficient (k) of the glasses.

3.5.1. Mass attenuation coefficients

The experimental and calculated mass attenuation coefficients of glasses are listed in Table 3 and illustrated, as a function of photon energy, for S (without La) and S5 (with maximum La content) glasses in Fig. 7. The results for the $(\mu_m)_{Exp.}$ are in excellent agreement with the calculated data. It can also be noted from Figs. 7 and 8A that the mass attenuation coefficients of the glass is varied with chemical composition and decreases with increasing photon energy.

For comparison, the μ_m values of various glasses have been normalized to S glass sample. Therefore, Fig. 8B presents $(\mu_m)_R$: the ratio ofμ_m a glass to μ_m of the S sample. Observation of this figure shows that the glass with higher La_2O_3 content have μ_m values systematically greater than that of S over the studied energy range. Similar findings were reported by Kilicoglu et al. (2019). La_2O_3 content can dramatically increase the μ_m value (≈350% for S5 around 100 keV) or it can significantly increase it (≈25% for S5) in high energy region as shown in Fig. 8B.

It is also seen that $(\mu_m)_R$ is approximately unity at intermediate energies, where Compton scattering is the dominating interaction process. This finding reflects the fact that when Compton scatter is the predominant interaction then equal masses of various materials gives almost the same Compton attenuation in units of (cm^2/g). A similar behavior were observed for all gamma-ray attenuation parameters which based on the mass attenuation coefficient as shown in the next sections.

Fig. 9 shows the correlation between the glass density and experimental attenuation coefficient of γ-ray. As has been reported, γ-ray shielding ability is strongly dependent on the density of material (Sikora et al., 2019). For instant, the μ_m values of S (3.914 g/cm^3) and S5 (4.184 g/cm^3) were 0.4226 cm^2/g and 1.2823 cm^2/g, respectively, at 0.08 MeV.

3.5.2. Half-value layer

As seen in Figs. 7 and 8A, mass attenuation coefficient decreases with the increase in photon energy, which means that a thicker material is needed to compensate for the decrease in μ_m. So, it is helpful to express the attenuation ability of a substance in terms of a half-value layer (HVL). The HVL is the thickness of the interacting material that reduces the intensity of radiation to half. In terms of thickness requirement, a lower value of HVL means that a better radiation shielding material. The theoretically calculated and experimentally determined values are given in Table 4. Fig. 10A and Table 4 clearly indicate that glass with higher La_2O_3 content has lower HVL and consequently thickness of the glass needs to be decreased. This effect can be represented visually with the use of the normalized thickness values (HVL) with respect to the S glass as shown in Fig. 10B. For high energy photons, the HVL of S5 sample is lowered noticeably (about 20%) compared with S sample. Fig. 10A also reveals that HVL values are nearly the same for all samples at intermediate photon energies 0.72–3.16 MeV and their maximum values were noticed around 10 MeV. This behavior can be attributed to the relative dominance of Compton scattering and pair

Table 3
Experimental and calculated values of μ_m for the prepared samples.

Energy (MeV)	S			S1			S2		
	$\mu_m(cm^2/g)$		Dive.	$\mu_m(cm^2/g)$		Dive.	$\mu_m(cm^2/g)$		Dive.
	Exp.	Cal.	%	Exp.	Cal.	%	Exp.	Cal.	%
0.08	0.4226	0.4234	0.18	0.6005	0.5963	−0.71	0.7665	0.7692	0.36
0.256	0.1200	0.1215	1.21	0.1296	0.1282	−1.05	0.1340	0.1348	0.59
0.662	0.0758	0.0758	−0.04	0.0770	0.0760	−1.29	0.0762	0.0763	0.14
1.173	0.0571	0.0572	0.10	0.0579	0.0571	−1.45	0.0572	0.0570	−0.35
1.333	0.0536	0.0535	−0.02	0.0543	0.0534	−1.70	0.0533	0.0533	−0.06
Energy (MeV)	S3 $\mu_m(cm^2/g)$ Exp.	Cal.	Dive. %	S4 $\mu_m(cm^2/g)$ Exp.	Cal.	Dive. %	S5 $\mu_m(cm^2/g)$ Exp.	Cal.	Dive. %
0.08	0.9407	0.9420	0.14	1.1150	1.1150	0.00	1.2823	1.2880	0.44
0.256	0.1413	0.1415	0.13	0.1482	0.1482	−0.02	0.1546	0.1549	0.18
0.662	0.0766	0.0766	0.01	0.0766	0.0769	0.39	0.0769	0.0772	0.31
1.173	0.0571	0.0569	−0.35	0.0569	0.0568	−0.25	0.0569	0.0567	−0.35
1.333	0.0532	0.0532	−0.06	0.0533	0.0531	−0.43	0.0532	0.0530	−0.34

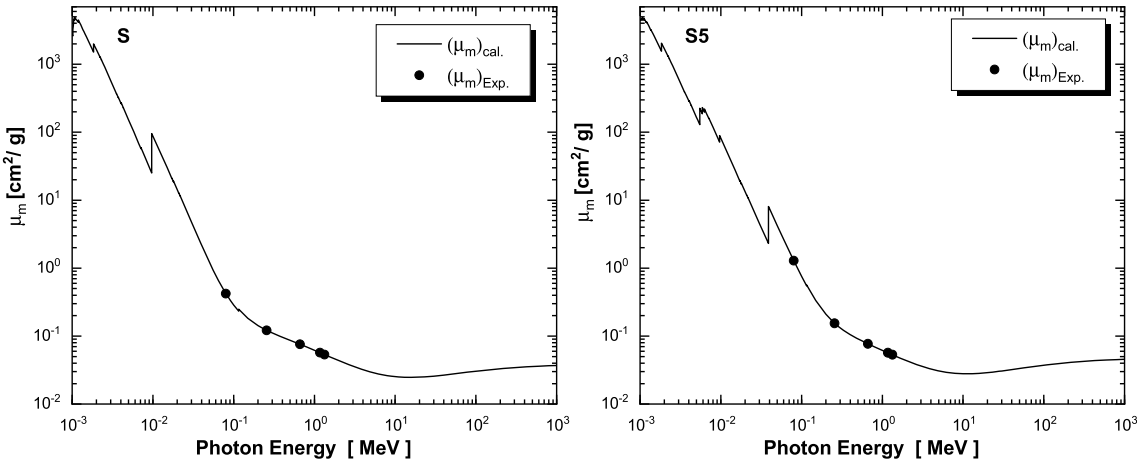

Fig. 7. Measured and calculated mass attenuation coefficients for S and S5 samples as a function of photon energy.

production processes for intermediate - and high-energy gammas. For instance, in S5 glass, Fig. 11 shows that the Compton scatter is the predominant interaction at intermediate energies and peaked at 1.25 MeV as well as the equality between Compton scatter and pair production process exists when the incident photon energy attains 10 MeV. Therefore, it can be concluded that the maximum value for HVL was recorded when the total interaction probability was equally divided between the Compton and pair production processes.

3.5.3. Effective atomic number

The effective atomic number and the effective density parameters are a convenient way for evaluation of gamma-ray interaction with compounds or mixtures. The effective electron density values are closely related to the effective atomic number [$N_{eff} = N_A Z_{eff} / < A >$ where N_A is the Avogadro's number and $<A>$ is the average atomic mass of the material] (Manohara et al., 2009). As a consequence, the qualitative energy dependence of N_{eff} is very similar to that of Z_{eff} and as a result only Z_{eff} values are presented here.

Table 5 presents the experimental and theoretical values of the effective atomic numbers for the glasses and an excellent agreement was observed. Fig. 12A is also displaying the effective atomic numbers for the prepared samples as a function of photon energy. All samples have almost the same trand which mirrors the dominance of partial interaction processes (Manohara et al., 2009). As a consequence, the qualitative energy dependence of N_{el} is very similar to that of Z_{eff} and as a result only Z_{eff} values are presented here.

Table 5 presents the experimental and theoretical values of the

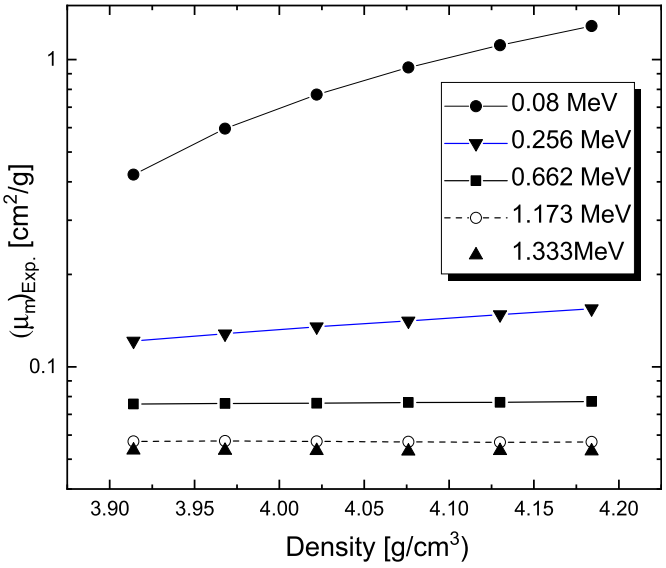

Fig. 9. Variation of experimental mass attenuation coefficients with glass densities at photon energy 0.080–1.333 MeV.

effective atomic numbers for the glasses and an excellent agreement was observed. Fig. 12A is also displaying the effective atomic numbers for the prepared samples as a function of photon energy. All samples have almost the same trend which mirrors the dominance of partial

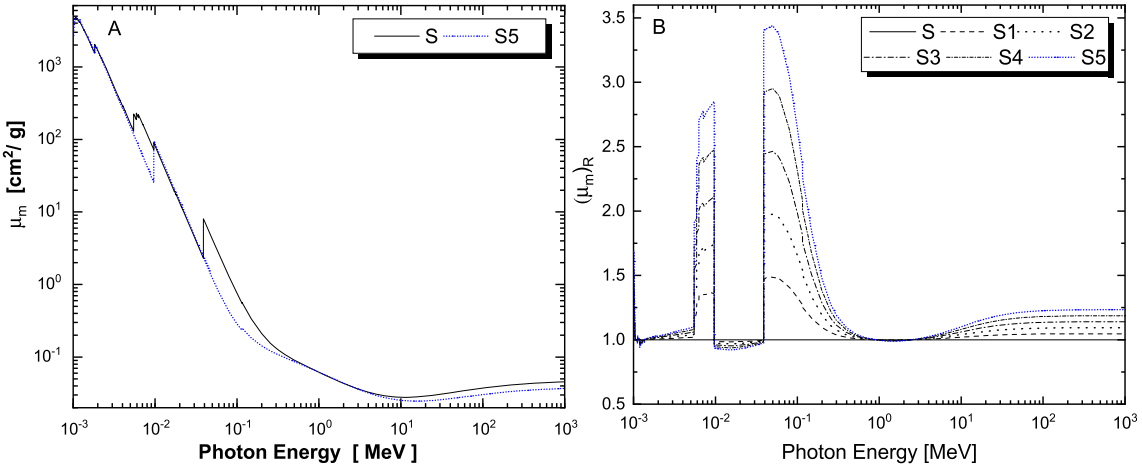

Fig. 8. (A) Mass attenuation coefficients of S and S5 glasses and (B) $(\mu_m)_R$ the ratio of μ_m values of various glasses with those of the S glass, as a function of energy.

Table 4
Experimental and calculated values of HVL (cm) at different photon energies (MeV) for the prepared samples.

E_γ	S		S1		S2		S3		S4		S5	
	Exp.	Cal.	Exp.	Cal.	Exp.	Cal.	Exp.	Cal.	Exp.	Cal.	Exp.	Cal.
0.08	1.64	1.64	1.16	1.16	0.90	0.90	0.74	0.74	0.62	0.62	0.54	0.54
0.256	5.71	5.70	5.41	5.41	5.14	5.14	4.91	4.90	4.69	4.68	4.49	4.47
0.662	9.15	9.15	9.13	9.12	9.11	9.08	9.06	9.05	9.04	9.01	8.99	8.98
1.173	12.12	12.13	12.10	12.15	12.13	12.17	12.17	12.19	12.21	12.21	12.18	12.23
1.333	12.95	12.95	12.98	12.97	13.01	13.00	13.04	13.03	13.00	13.06	13.03	13.08

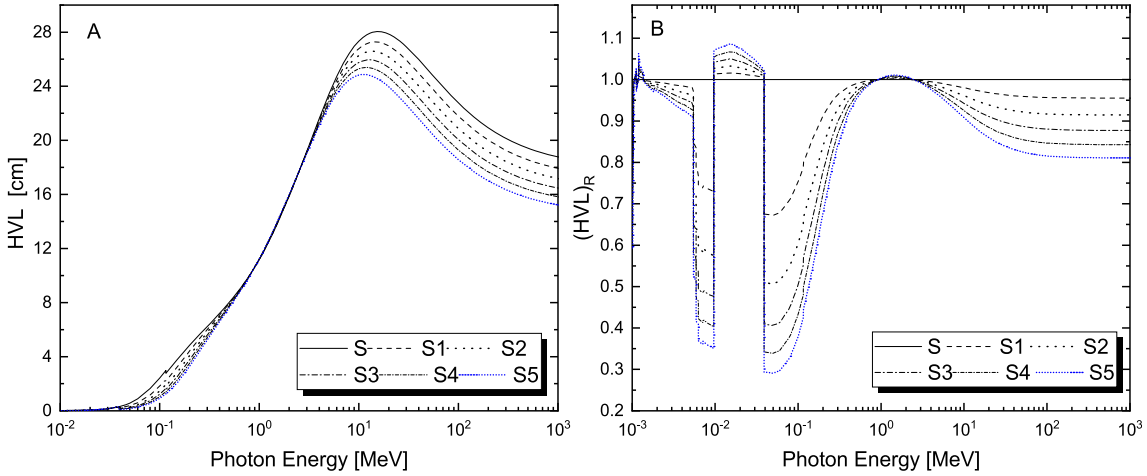

Fig. 10. (A) Half-value layer (HVL) of all glasses and (B) $(HVL)_R$ the ratio of HVL values of various glasses with those of the S glass, as a function of energy.

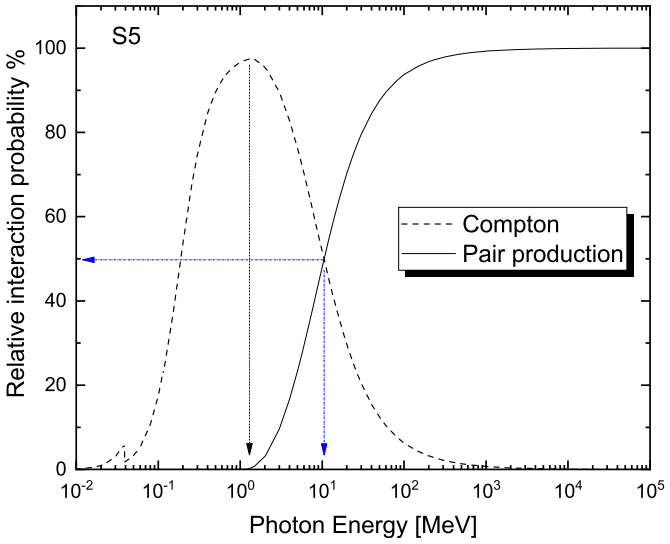

Fig. 11. Relative interaction probabilities of Compton scatter and pair production process, as a function of energy.

interaction processes (Manohara et al., 2009). In Fig. 12, one can clearly notice that the curves of Z_{eff} are arranged in ascending order according to their La_2O_3 content, (cf. Table 1, row #6).

Fig. 12B gives the ratio of Z_{eff} of the glasses to Z_{eff} of S sample. Differences are larger at lower and higher energies because of the dominance of photoelectric absorption and pair production, respectively. The maximum difference is observed around 100 keV for all the samples, as well as the percentage difference is as large as 29% for S5 glass at the high photon energy.

3.5.4. *Kerma coefficient k*

The kerma coefficient *k* signifies that the interaction of neutron and gamma radiations with matter is associated with heating production. The nuclear heating is sum of neutron heating and gamma heating. Gamma-ray heating is the local energy deposition from different gamma interaction processes, the most important of which are photoelectric, Compton and pair production (Zhang and Abdou, 1997). The precise knowledge of *k* found its utility in many applications, particularly fusion systems. The procedure for determination of the gamma-ray kerma coefficient was previously described by El-Khayatt (2017). The theoretical calculated and the experimentally determined values for *k* are presented in Table 6. The kerma coefficients of both glass systems S and S5 are shown in Fig. 13. It is found that the *k* of the S5 sample have

Table 5
Experimental and calculated values of Z_{eff} (e/atom) at different photon energies (MeV) for the prepared samples.

E_γ	S		S1		S2		S3		S4		S5	
	Exp.	Cal.	Exp.	Cal.	Exp.	Cal.	Exp.	Cal.	Exp.	Cal.	Exp.	Cal.
0.08	18.73	18.84	24.72	24.03	28.31	28.32	31.89	31.94	35.2	35.10	37.56	37.67
0.256	12.60	12.69	13.18	13.40	14.02	14.23	14.79	15.01	15.54	15.77	16.15	16.45
0.662	11.92	11.90	12.06	12.09	12.31	12.28	12.54	12.48	12.74	12.69	12.96	12.89
1.173	11.80	11.79	11.98	12.16	12.16	12.10	12.32	12.23	12.48	12.39	12.63	12.53
1.333	11.83	11.82	11.96	11.95	12.11	12.01	12.28	12.22	12.45	12.37	12.61	12.51

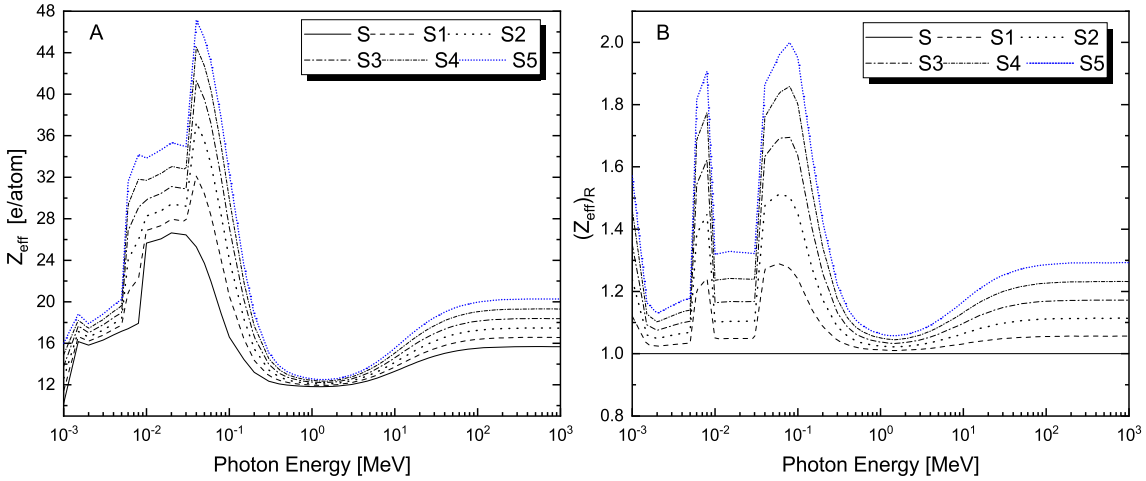

Fig. 12. (A) Effective atomic number (Z_{eff}) of all glasses and (B) $(Z_{eff})_R$ the ratio of Z_{eff} values of various glasses with those of the S glass, as a function of energy.

Table 6
Experimental and calculated values of kerma coefficients (pGy-cm^2/photon) at different photon energies (MeV) for the prepared samples.

E_γ	S		S1		S2		S3		S4		S5	
	Exp.	Cal.	Exp.	Cal.	Exp.	Cal.	Exp.	Cal.	Exp.	Cal.	Exp.	Cal.
0.08	3.36	3.37	5.53	5.52	7.69	7.68	9.84	9.85	12.00	12.00	14.16	14.15
0.256	1.50	1.50	1.77	1.76	2.03	2.03	2.30	2.29	2.56	2.56	2.83	2.82
0.662	3.10	3.10	3.14	3.14	3.19	3.18	3.23	3.23	3.28	3.27	3.32	3.32
1.173	4.97	4.97	4.98	5.00	4.98	5.00	4.99	5.00	4.99	4.99	5.00	5.02
1.333	5.48	5.48	5.48	5.48	5.48	5.48	5.48	5.48	5.48	5.51	5.48	5.50

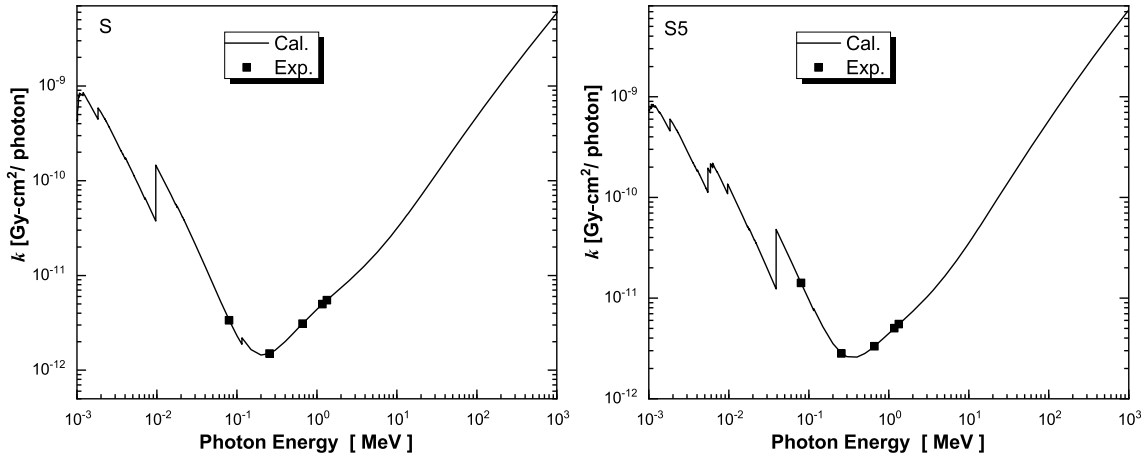

Fig. 13. Gamma-ray kerma coefficients (k) of S and S5 glasses, as a function of energy.

higher values than S glass as shown in Fig. 14A and B.

Normally, kerma coefficient curves reflect the dominance of various partial interactions, as a result of this, their values are larger at lower and higher energies due to the dominance of photoelectric absorption and pair production, respectively. It is seen that the plenty of K-, L- and M-absorption edges of the intermediate and high-Z elements (Fe, Zn, Zr, La and U) have, of course, considerably complicated the low-energy dependence of k. A similar situation exists in all pervious graphs for gamma-ray interaction parameters such as the mass attenuation coefficient, half-value layer and effective atomic numbers.

Differences among kerma coefficients of the glasses are illustrated in Fig. 14B and a significant disparity between samples is noticed. Also, the maximum difference is observed around 100 keV for all the glasses whereas the percentage difference which recorded at high energies is as large as 25% for S5 glass.

3.6. Macroscopic effective removal cross-section for fast neutrons (Σ_R)

Weight fractions of elemental composition for glasses were used as input data for NXCom program (El-Khayatt, 2011) to calculate the Σ_R(cm^{-1}) for all samples. It can be seen from Table 7 that there is a slight increase in the removal cross-section, Σ_R, with increase La_2O_3 content.

Fig. 15 shows the correlation between the glass density and the macroscopic removal cross-section of fast neutron. It is clearly seen that Σ_R increase with the increasing glass density. On the other hand, Σ_R/ρ increased linearly with the weight percentage of the moderator elements ($A \leq 16$) in glass as shown in Fig. 16.

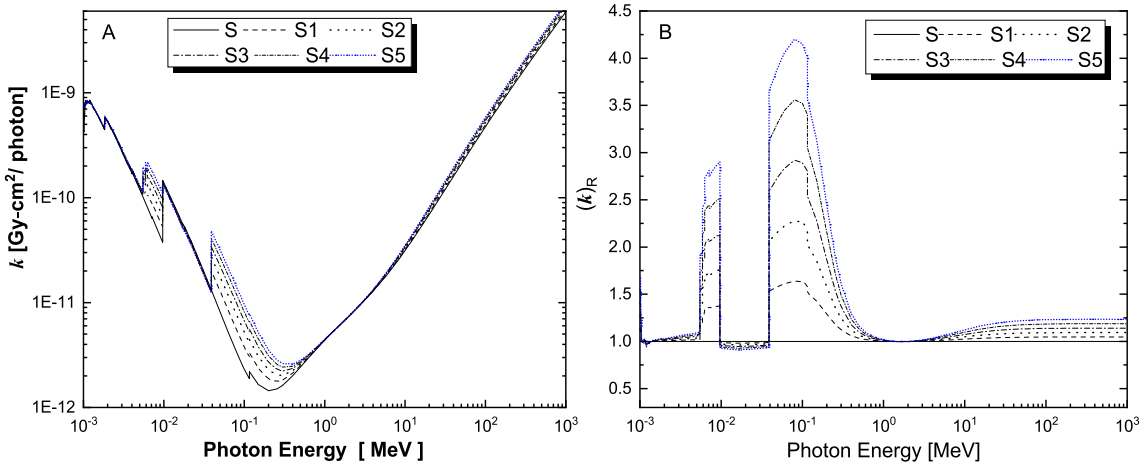

Fig. 14. (A) Gamma-ray kerma coefficients (k) of all glasses and (B) $(k)_R$ the ratio of k values of various glasses with those of the S glass, as a function of energy.

Table 7
Moderator (A ≤ 16) contents (wt.%) and the calculated values of Σ_R (cm^{-1}) for the studied glasses and SCC and BMC as a standard radiation shielding material.

The quantity	Sample glass						Concrete	
	S	S1	S2	S3	S4	S5	SCC	BMC
Wt%(moderator)	65.01	64.72	64.42	64.13	63.83	63.54	34.17	64.1
Σ_R (cm^{-1})	0.12114	0.12141	0.12165	0.12184	0.12200	0.12213	0.11728	0.10280

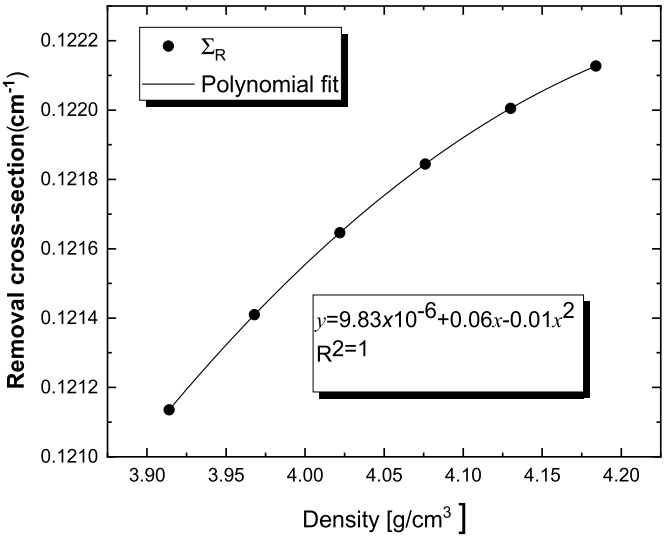

Fig. 15. Variation of removal cross-section with glass densities.

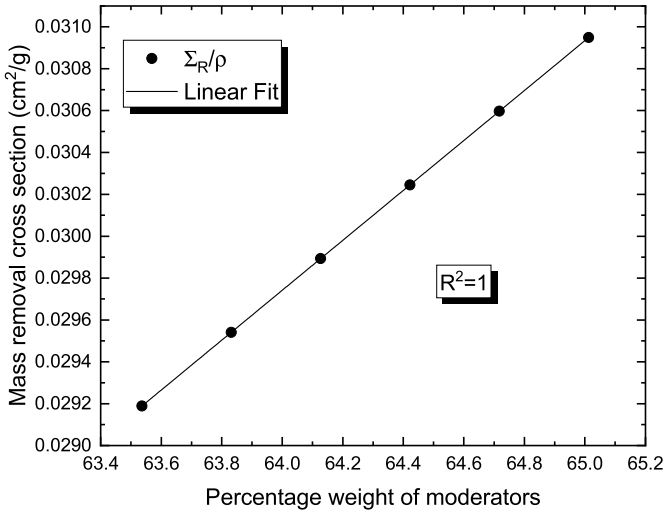

Fig. 16. Variation of mass removal cross-section with moderator weight fractions.

3.7. Comparisons with standard radiation shielding materials

The composition and density data of basalt magnetite concrete (BMC) and steel scrap concrete (SSC) as a standard radiation shielding material, were obtained from literatures (Bashter, 1997) and their mass attenuation coefficients and removal cross-sections were calculated. Removal cross-section data of BMC and SSC are presented in Table 7 for comparison. The obtained results showed that the removal cross-sections of fast neutrons of the prepared glass are slightly higher than those of the SSC and BMC. This finding is consistent with the fact that high-Z additives leading to a higher density and consequently causing an enhancement in Σ_R values.

Fig. 17A and B give the ratio of μ_m (the most fundamental attenuation parameter) of the S5 glass to μ_m of BMC and SSC, respectively. Observation of Fig. 17 shows that S5 glass, the glass with higher La content, has μ_m values systematically greater than that of BMC and SSC over the full energy range, as well as the maximum and the minimum differences were, respectively, recorded at low and high photon energies. Therefore, it can be concluded that the S5 glass gives better attenuation performance than BMC and SSC concretes.

4. Conclusions

In this study six glass systems, [x La_2O_3 (40-x) ZnO10Na_2O10B_2O_3 40 WSS] where x = 0, 6, 12, 18, 24 and 30 wt%) were prepared by melt quench method and the XRD results confirmed that the obtained glasses are amorphous. A comparative study among these glass systems have been carried out for their physical and radiation shielding properties. From the theoretical and the experimental obtained results, the following conclusions can be drawn:

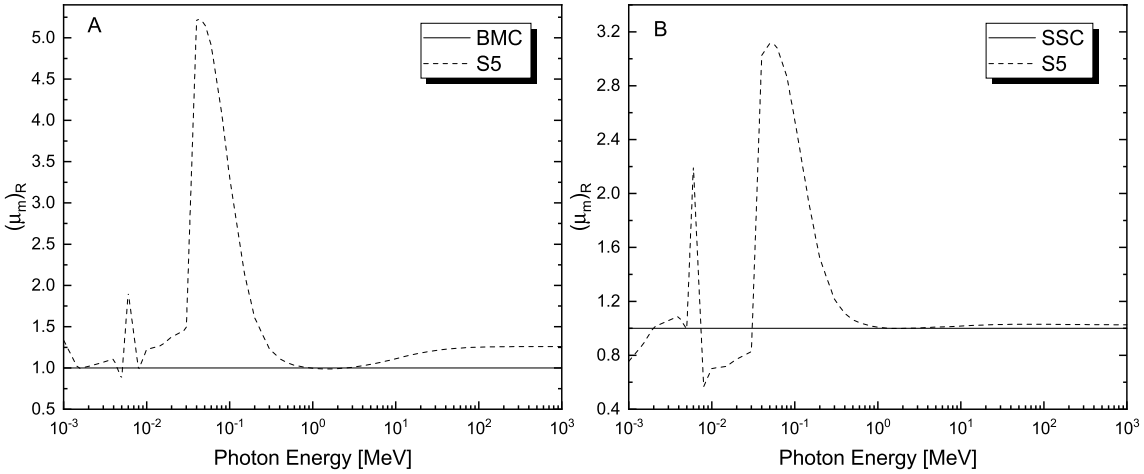

Fig. 17. $(\mu_m)_R$: the ratio of μ_m values of S5 with those of (A) BMC and (B) SSC, as a function of energy.

1) The investigation of the physical properties of the prepared glasses proved that the substitution of ZnO by La_2O_3 contributes to a linear increase in both density and hardness. As well as the oxygen packing density is increased too, which indicates that the glass network is going to be more tightly packing.
2) The transmission increases gradually with increasing the La_2O_3 content. S5 shows a high percentage of transmittance in the visible area of spectra (650–1000 nm) exceeds 80%.
3) Generally, the replacement of ZnO with La_2O_3 significantly improvement the γ-shielding properties of glass systems, and this effect is especially pronounced in low (around 100 keV) and high (beyond 10 MeV) energy regions.
4) The attenuation parameters of S5 glass, with maximum La addition, are is significantly superior to the others. Namely, μ_m, Z_{eff} and k values of S5 glass exhibited a significantly increase, at high energy, 25%, 29% and 25%, respectively. In addition, the HVL values of S5 is lowered by 20% in compared to the S sample beyond the intermediate energy region.
5) HVL values are nearly the same for all samples at intermediate photon energies 0.72–3.16 MeV, as well as the maximum value for HVL was observed when the total interaction probability being equally divided between Compton scatter and pair production process.
6) A comparison of μ_m and Σ_R for the prepared glass and SSC and BMC shows that the S5 have superior shielding properties, making it more efficient in a mixed gamma-neutron environment.
7) The prepared glass systems are promising radiation shielding material due superiority of shielding properties, transparency and leadfree shielding material.
8) For the current glass networks, La is a good substitute for Zn in order to improve both physical and radiation-shielding properties.

Appendix A. Supplementary data

Supplementary data to this article can be found online at https://doi.org/10.1016/j.radphyschem.2019.108497.

References

Abouhaswa, A.S., Rammah, Y.S., Sayyed, M.I., Tekin, H.O., 2019. Synthesis, structure, optical and gamma radiation shielding properties of B2O3-PbO2-Bi2O3 glasses. Compos. B Eng. 172, 218–225.
Alallak, N.A., Sarhan, S.S., 2012. Factors affecting gamma ray transmission. Jordan J. Phys. 5 (2), 77–88.
Alharbi, T., Mohamed, Hamdy F.M., Saddeek, Yasser B., El-Haseib, Ahmed Y., Shaaban, Kh S., 2019. Study of the TiO2 effect on the heavy metals oxides borosilicate glasses structure using gamma-ray spectroscopy and positron annihilation technique. Radiat. Phys. Chem. 164, 108345.
Bashter, I.I., 1997. Calculation of radiation attenuation coefficients for shielding concretes. Ann. Nucl. Energy 24, 1389–1401.
Blizard, E.P., Abbott, L.S., 1962. Reactor Handbook Vol. III John Wiley & Sons, Inc Part B, Shielding.
El-Khayatt, A.M., 2011. NXcom - a program for calculating attenuation coefficients of fast neutrons and gamma-rays. Ann. Nucl. Energy 38 (1), 128–132.
El-Khayatt, A.M., 2017. Semi-empirical determination of gamma-ray kerma coefficients for materials of shielding and dosimetry from mass attenuation coefficients. Prog. Nucl. Energy 98, 277–284. https://doi.org/10.1016/j.pnucene.2017.04.006.
El-Khayatt, A.M., Akkurt, I., 2013. Photon interaction, energy absorption and neutron removal cross section of concrete including marble. Ann. Nucl. Energy 60, 8–14.
El-Khayatt, A.M., Vega-Carrillo, H.R., 2015. Photon and neutron kerma coefficients for polymer gel dosimeters. Nucl. Instrum. Methods Phys. Res. 792, 6–10.
Esra, Kavaz, 2019. An experimental study on gamma ray shielding features of lithium borate glasses doped with dolomite, hematite and goethite minerals. Radiat. Phys. Chem. 160, 112–123.
Gerward, L., Guilbert, N., Jensen, B., Levring, H., 2004. WinXCom-program for calculating X-ray attenuation coefficients. Radiat. Phys. Chem. 71, 653–654.
Hubbell, J.H., Seltzer, S.M., 1995. Tables of X-Ray Mass Attenuation Coefficients and Mass Energy-Absorption Coefficients 1 KeV to 20 MeV for Elements Z ¼ 1 to 92 and 48 Additional Substances of Dosimetric Interest NISTIR 5632. National Institute of Standards and Technology, Gaithersburg.
Junior, T.A.A., Nogueira, M.S., Vivolo, V., Potiens, M.P.A., Campos, L.L., 2017. Mass attenuation coefficients of X-rays in different barite concrete used in radiation protection as shielding against ionizing radiation. Radiat. Phys. Chem. 140, 349–354.
Kaplan, M.F., 1989. Concrete Radiation Shielding. John Wiley and Sons, Inc., New York.
Rajinder Singh, Kaundal, 2016. Comparative study of radiation shielding parameters for bismuth borate glasses. Mater. Res. 19 (4), 776–780.
Kilicoglu, O., Altunsoy, E.E., Agar, O., Kamislioglu, M., Sayyed, M.I., Tekin, H.O., Tarhan, N., 2019. Synergistic effect of La_2O_3 on mass stopping power (MSP)/projected range (PR) and nuclear radiation shielding abilities of silicate glasses. Results in Physics 14, 102424.
Kim, N.J., La, Y.H., Im, S.y., Han, W.T., Ryu, B.K., 2009. Effect of ZnO on physical and optical properties of bismuth borate glasses. Electr. Mater Lett. 5 (4), 209–212.
Kirdsiri, K., Kaewkhao, J., Chanthima, N., Limsuwan, P., 2011. Comparative study of silicate glasses containing Bi2O3, PbO and BaO: radiation shielding and optical properties. Ann. Nucl. Energy 38 (6), 1438–1441.
Limkitjaroenporn, P., Kaewkhao, J., Asavavisithchai, S., 2013. Determination of mass attenuation coefficients and effective atomic numbers for Inconel 738 alloy for different energies obtained from Compton scattering. Ann. Nucl. Energy 53, 64–68.
Liu, Z., Chen, J., 2008. New calculations of neutron kerma coefficients and dose equivalent. J. Radiol. Prot. 28 (2), 185–193.
Manohara, S.R., Hanagodimath, S.M., Gerward, L., 2009. Photon interaction and energy absorption in glass: a transparent gamma ray shield. J. Nucl. Mater. 393, 465–472.
Oliveira, L A Pereira De, 2008. Mechanical and durability properties of concrete with ground waste glass sand. In: 11DBMC International Conference on Durability of Building Materials and Components 1.
Saddeek, Y.B., Shaaban, K.H.S., Elsaman, Reda, Atef El-Taher, Amer T.Z., 2018. Attenuation-density anomalous relationship of lead alkali borosilicate glasses. Radiat. Phys. Chem. 150, 182–188.
Saudy, H.A., El Mosallamy, S., El Kameesy, S.U., Sheta, N., Mostafa, A.G., Sallam, A.H., 2013. Mechanical, thermal and chemical durability behaviors of CdO-Bi_2O_3 borophosphate glasses containing Fe_2O_3. World J. Condens. Matter Phys. 3 (1), 9–13.
Sayyed, M.I., Tekin, H.O., Agar, O., 2019. Gamma photon and neutron attenuation properties of MgO–BaO–B2O3–TeO2–Cr2O3 glasses: the role of TeO_2. Radiat. Phys. Chem. 163, 58–66.
Shamshad, L., Rooh, G., Limkitjaroenporn, P., Srisittipokakun, N., Chaiphaksa, W., Kim, H.J., Kaewkhao d, J., 2017. A comparative study of gadolinium based oxide and oxyfluoride glasses as low energy radiation shielding materials. Prog. Nucl. Energy 97, 53–59.

Sikora, P., Abd Elrahman, M., Horszczaruk, E., Brzozowski, P., Stephan, D., 2019. Incorporation of magnetite powder as a cement additive for improving thermal resistance and gamma-ray shielding properties of cement-based composites. Constr. Build. Mater. 204, 113–121.

Singh, S., Kumar, A., Sing, D., Thind, K.S., Mudahar, G.S., 2008. Barium–borate–flyash glasses: as radiation shielding materials. Nucl. Instrum. Methods Phys. Res. B 266, 140–146.

Singh, Gurinder Pal, Kaur, Parvinder, Kaur, Simranpreet, Singh, D.P., 2014. Gamma ray effect on the covalent behaviour of the CeO2 – BaO – B2O3 glasses. Physica B: Phys. Condens. Matter 450, 106–110.

Singh, Anod Kumar, et al., 2017. Effect of La_2O_3 concentration on structural , optical and cytotoxicity behaviours of strontium titanate borosi. J. Non-Cryst. Solids 481, 176–183.

Smiljanić, S.V., Grujić, S.R., Tošić, M.B., Živanović, V.D., Matijašević, S.D., Nikolić, J.D., Topalović, V.S., 2015. Effect of La2O3 on the structure and the properties of strontium borate glasses. Chem. Ind. Chem. Eng. Q. 22 (1), 111–115.

Un, A., Demir, F., 2013. Determination of mass attenuation coefficients, effective atomic numbers and effective electron numbers for heavy-weight and normal-weight concretes. Appl. Radiat. Isot. 80, 73–77.

Zhang, L., Abdou, M.A., 1997. Kerma factor evaluation and its application nuclear heating experiment analysis. Fusion Eng. Des. 36, 479–503.